Detection of reflections in GNSS radio occultation measurements using phase matching

Thomas Sievert[1], Joel Rasch[2], Anders Carlström[3], and Mats I. Pettersson[1]

[1]Blekinge Institute of Technology, Karlskrona, Sweden
[2]Molflow, Gothenburg, Sweden
[3]RUAG Space AB, Gothenburg, Sweden

Correspondence to: Thomas Sievert (thomas.sievert@bth.se)

Abstract. It is well-known that in the presence of super-refractive (SR) layers in the lower troposphere inversion of GNSS radio occultation (RO) measurements using the Abel transform yields biased refractivity profiles. As such it is problematic to reconstruct the true refractivity from the RO signal. Additional information about this lower region of the atmosphere might be embedded in reflected parts of the signal. To retrieve the bending angle, the phase matching operator can be used. This operator

5   produces a complex function of the impact parameter, and from its phase we can calculate the bending angle. Instead of looking at the phase, in this paper we focus on the function's amplitude. The results in this paper show that the signatures of surface reflections in GNSS RO measurements can be significantly enhanced when using the phase matching method by processing only an appropriately selected segment of the received signal. We can then identify reflection signatures even in cases where they are normally obscured by the direct signal's influence on the phase matching amplitude. This signature enhancement is

10 demonstrated by simulations and confirmed with real MetOp-A data.

1   Introduction

GNSS radio occultation (RO) is a technique used for sounding the Earth's atmosphere. Assuming spherical symmetry of the atmosphere, the bending angles of GNSS signals passing through the atmosphere can be found and assimilated into numerical weather prediction (NWP) systems. The bending angle measurements contain valuable information due to their relation to the

15 atmosphere's refractivity, which can yield information about humidity, temperature and pressure (e.g., Kursinski et al., 2000; Yunck et al., 2000). The geometry of transmitter, Earth, and receiver, as well as the short wavelength of the signals, result in a measurement with high vertical resolution. In many RO events, the atmosphere is sounded above a region of the Earth where the surface reflects the signal. This results in reflected parts of the signal also being received by the RO instrument in orbit. Boniface et al. (2011) have shown that reflected signals contain meteorological information. A method to detect these reflected

20 components was suggested by Hocke et al. (1999) and has later been used on real data and shown to work (e.g., Beyerle et al., 2002; Pavelyev et al., 2002). This method uses a radio hologram generated by subtracting a ray traced reference field from the received signal. An analysis of reflection signatures in GNSS RO data was performed by Gorbunov (Gorbunov, 2016), where the canonical transform method was used for processing the data. Some investigations have been made into whether these reflections can improve the quality of RO data (Cardellach and Oliveras, 2016). While occultations with recorded reflections

seem to be of higher quality than ones without, a binary reflection flag is probably not appropriate for assimilation purposes, since the potential improvement varies depending on geographical location. (Healy, 2015).

When receiving a RO signal, we use the phase matching (PM) operator (Jensen et al., 2004), which outputs a complex function of impact parameter whose phase is proportional to the signal's bending angle. Although the amplitude of this function may contain valuable information as well, it has not been appropriately investigated.

In this paper, we compare the phase matching amplitudes of simulated measurements to real measurements made by the GRAS instrument aboard MetOp-A. We demonstrate signatures corresponding to surface reflections, and propose a method to distinguish them from the much stronger signatures of the direct signal. We motivate this method using simulated data and a simple geometric model for where reflected components are expected to appear in the signal. Finally we discuss the difference in structure between simulated and real signals, as well as the potential future uses of the PM amplitude.

2 Phase matching

Jensen et al. define PM as an operator that transforms a complex signal of time $u(t)$ to impact parameter space:

$$U(a) = \int\limits_{t_{min}}^{t_{max}} u(t) \exp\left(-ik_0 S(t,a)\right) dt \tag{1}$$

Here, k is the wave number of the GNSS signal, $S(t,a)$ is the optical path length of a model ray path, and a is impact parameter. The derivative of $arg(U(a))$ with respect to a is proportional to the bending angle. As this integral is defined for any impact parameter a, it is important to determine at which a the function does not contain relevant information anymore. The lowest a is usually around 2.1 km above the radius of the Earth's curvature, which corresponds to a surface refractivity of approximately 330 refractive units. To make sure that all information in the signal is mapped to impact parameter space, we compute the U for impact parameter values going all the way to the Earth's surface. This also ensures that we include reflected rays in the U function. It is not obvious that the PM method should work for reflected rays, as the geometrical model ray path is constructed for a direct ray, but in the appendix it is shown that the standard phase matching technique works perfectly well to use on reflected rays, provided the Earth surface is smooth.

3 A model for reflected rays

In Fig. 1 we demonstrate that the features we see in the amplitude for the complex function U are actually caused by reflections; by overlaying a curve for the predicted straight line tangent altitude (SLTA) as a function of impact height for the direct rays (blue line), and reflected rays (red line). The black lines show the amplitude of the U function when passing segments of the signal to the PM operator using a a 10 km sliding window. This model is qualitative, and we use the simplification of assuming

that the orbital radii for the satellites are fixed, and that the Earth surface is completely smooth. In the appendix it is shown that the bending angle for a reflected ray (provided the Earth surface is smooth) is given by

$$\alpha(a) = -2a \int\limits_{R_E n(R_E)}^{\infty} \frac{1}{\sqrt{r^2 n^2 - a^2}} \frac{d\ln n}{dr} dr - \pi + 2\arcsin\left(\frac{a}{R_E n(R_E)}\right). \tag{2}$$

Where α is the bending angle, R_E the Earth radius of curvature, and n the refractive index as a function of radius. The bending
5 angle of a direct ray is given by the same expression without the last two terms. The integral can be evaluated numerically using the method described in (Rasch, 2014). The SLTA for fixed values of the LEO and GNSS orbital radii is given by

$$SLTA = \frac{r_L r_G \sin\theta}{\sqrt{r_L^2 + r_G^2 - 2r_L r_G \cos\theta}} - R_E \tag{3}$$

Where r_L and r_G are the LEO and GNSS orbit radii, and θ is the separation angle between the satellites, given by

10 $$\theta = \pi + \alpha - \arcsin\left(\frac{a}{r_L}\right) - \arcsin\left(\frac{a}{r_G}\right) \tag{4}$$

4 MetOp-A data

The data from occultation events is collected from the COSMIC Data Analysis and Archive Center (CDAAC) web interface, specifically day 2007.274 with the metopa2016 designation, indicating reprocessed measurements from MetOp-A. The signal amplitude, excess phase and orbit data needed for PM are all found in the atmPhs files. In these files, the orbit coordinates
15 are given with the Earth's center of mass as the point of origin. To get more accurate values of impact height, we translate the coordinates so that they instead consider the center of curvature of the Earth at the occultation point. This is done by collecting translation data from the corresponding atmPrf files. As the atmPrf files contain bending angle and impact height values, these were used to control the accuracy of the PM implementation.

For simulating a GNSS signal as it passes through the atmosphere, a wave optics propagator (WOP) is used with the multiple
20 phase screen technique (see e.g., Benzon et al., 2003; Benzon and Gorbunov, 2012; Rasch, 2014). To make simulations similar to the simpler geometry of the WOP, the GNSS transmitter position is set at a distance corresponding to the mean value of the distance between the center of curvature and the actual GNSS position in the CDAAC data file. Similarly, the receiver satellite orbit is assigned a constant radius. To determine the length of the orbit (how deep the occultation goes), the minimum and maximum separation angles between transmitter and receiver are computed and used. These values can be modified to
25 simulate a deeper occultation event. For an atmosphere, the high-resolution, co-located refractivity profile from ECMWF also provided by CDAAC is used (echPrf files). These profiles do not go all the way to the ground - the last bit is extrapolated linearly. To simulate surface reflections, we set the electromagnetic field to 0 on all parts of the phase screens that lie inside
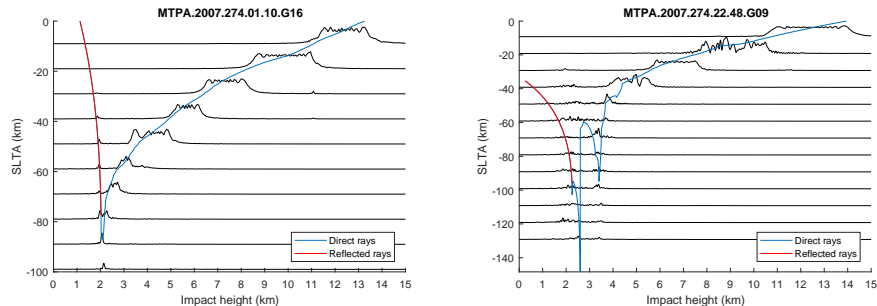
Figure 1. Using a sliding window for the signal yields PM amplitudes that correspond to the reflection model. Left shows a case with weak refractive gradients, right shows a case with strong refractive gradients.

the Earth. Although it is not clear whether this method has a solid physical basis it appears to give quite accurate results, and is routinley used in WOP simulations (Gorbunov, 2016; Levy, 2000).

5 Surface reflections

In the low part of the occultation (SLTA around -80 km, impact height around 2.1 km), where the signal becomes blocked by
5 the Earth, the magnitude of U also decreases. This decrease is very sharp in simulated data, and more varied in real signals. Around the a value that corresponds to the surface refractivity, there is sometimes a spike in $|U|$, even if the tracking was lost higher up. This spike is an indicator of the reflected signal. If tracking of the signal goes all the way to the surface, the spike overlaps with the direct signal and is obfuscated, as seen in Fig. (2). Figure (1) illustrates the relationship between the SLTA of the received signal and the specific rays for an exponential profile, represented by their impact heights. This shows that
10 reflected rays can be embedded at higher SLTAs than the lowest direct rays. It also implies that reflections that are otherwise hidden below a strong direct signal can be revealed by only performing PM on an orbital segment above a certain SLTA. To clearly identify the reflection spike and suppress the influence of the lowest direct rays, we pass a segment of the received signal to the PM operator. The reflection spike then arises on its own. The reflection spike then becomes clearly separated from the other parts of the signal. The sliding window used in Fig. (1) has a width of 10 km SLTA, and to avoid artifacts due to
15 the abrupt cutting of the signal the outer 5% of the window edges were tapered using a Tukey window (Tukey, 1967). Not performing such tapering would result in unwanted noise, seen in the truncated $|U|$ in Fig. (2).

6 Results

We present ten cases where PM is performed on real signals alongside their simulated counterparts based on ECMWF's co-located refractivity profiles. These cases are classified based on the sharpest gradient above 100 m, in the same manner as
20 the reference dataset from ECMWF (Healy, 2012). Overall, the structure of $|U|$ is similar to that of a step function, both
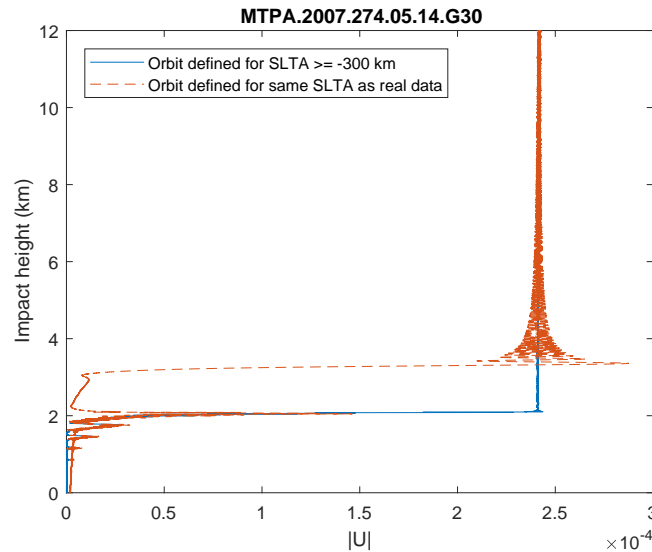
Figure 2. $|U|$ for a simulated signal that is propagated to a similar orbit as the real measurement (red), and one that is propagated to a deep orbit (blue). For illustration the truncated signal is not tapered, the dramatic oscillations seen slightly around 4 km is produced.

in simulations and using real data. By truncating the signals at an appropriate SLTA we can distinguish previously hidden reflection spikes in $|U|$. For this study we pick the altitude of truncation qualitatively. Figures (3) through (12) show the received signal (left), $|U|$ for a simulated signal (middle), and $|U|$ for the received signal (right). The plots are color coded so that the blue plots describe the complete signals, and the red plots describe the truncated signals.

5   Simulations on cases classified as category 3 and 4 - shown in Fig. (8) through (12) - give rise to a sharp, negative spike at an impact height corresponding to the sharp gradient in the refractivity profile. This structure cannot be found in the real data. Moreover, the real data shows a high level of noise that is not found in simulated data.

    We note that there are peculiar oscillating structures in the real data. Particularly in Fig. (4) at 6 km, Fig. (7) at 4 and 6 km, Fig. (8) at 7.5 km, Fig. (11) at 5 and 9 km, and in Fig. (12) at 5 and 9 km. These oscillating structures are not found in the

10 simulated data.

    While these ten hand-picked cases all clearly contain reflected components, there are several measurements in which the reflected parts cannot be distinguished. This is typically either because the measurement was not deep enough, or because $|U|$ was too noisy. For every measurement on this day that has mild noise in its $|U|$ function, there is always a reflection signature.
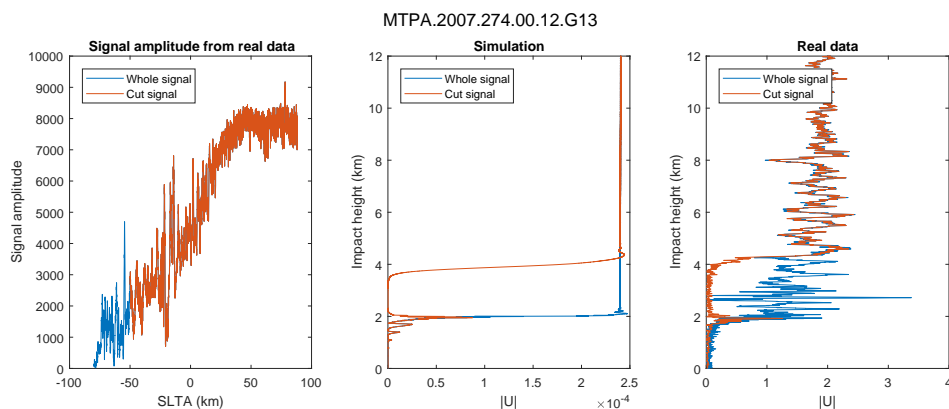
Figure 3. An event classified into category 1.
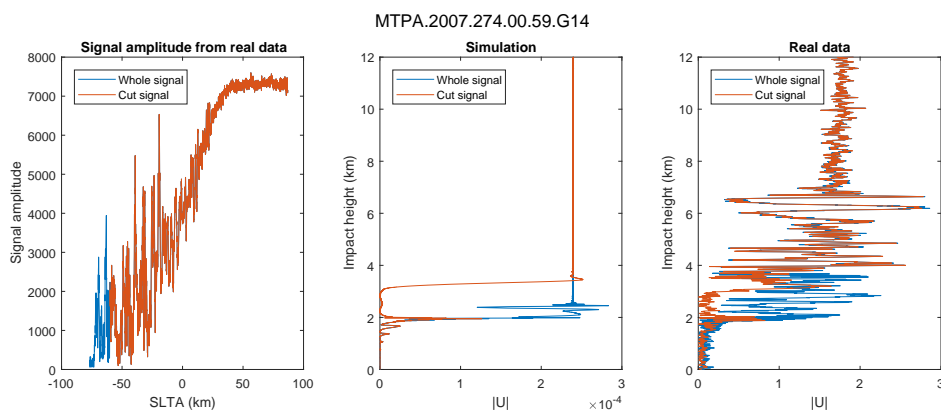
Figure 4. An event classified into category 1.
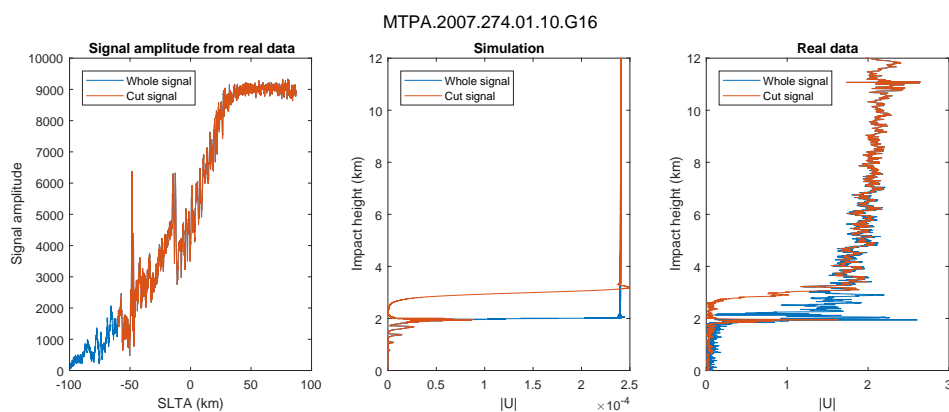
Figure 5. An event classified into category 1.
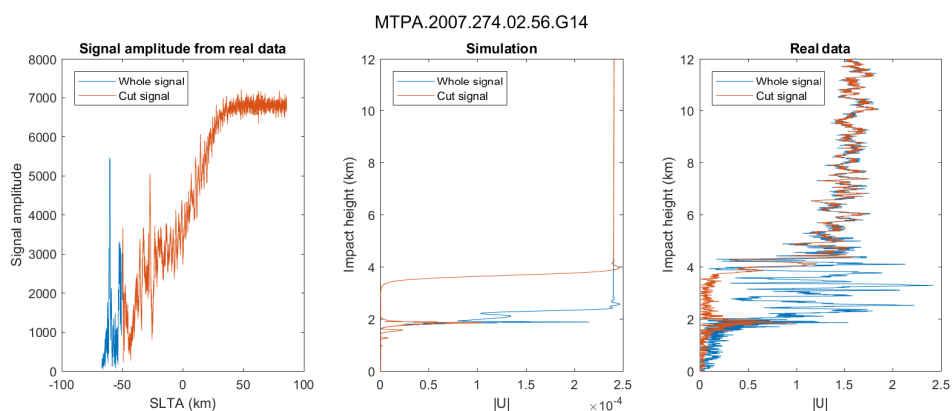
Figure 6. An event classified into category 1.
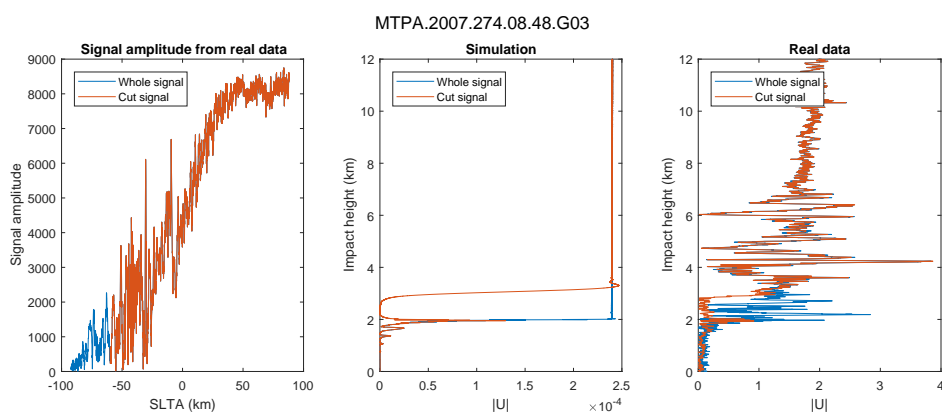
Figure 7. An event classified into category 1.
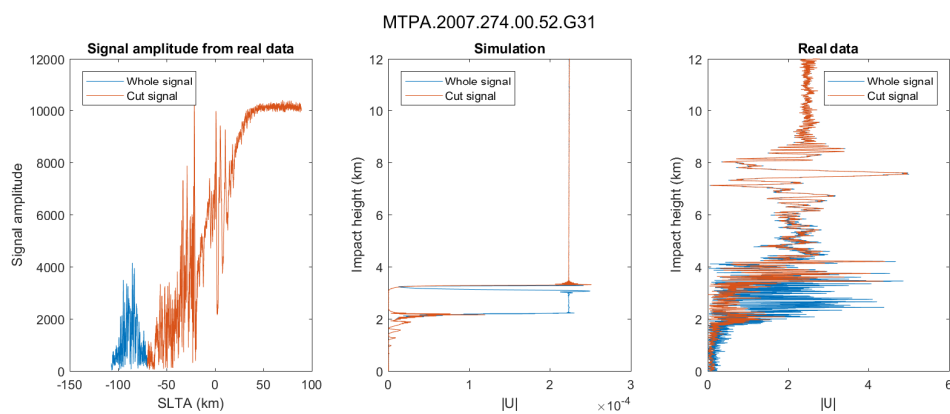
Figure 8. An event classified into category 3.
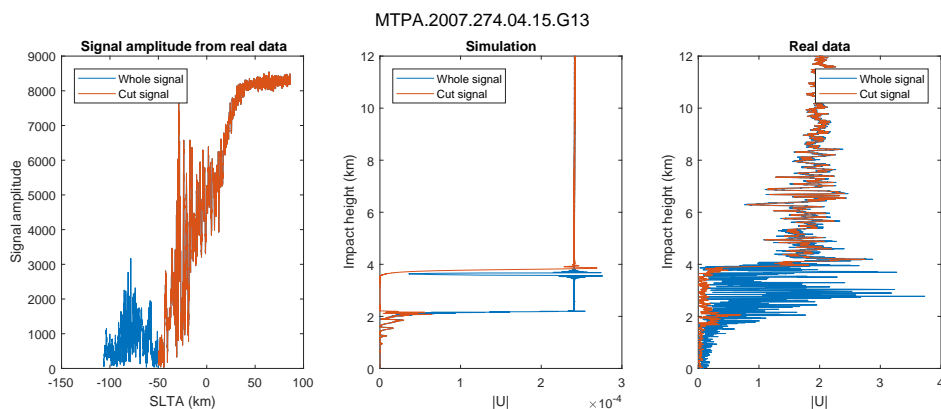
Figure 9. An event classified into category 3.
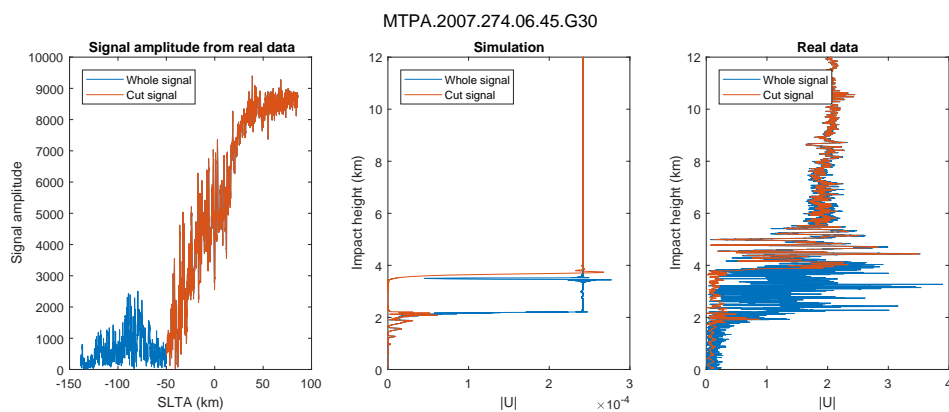
Figure 10. An event classified into category 3.
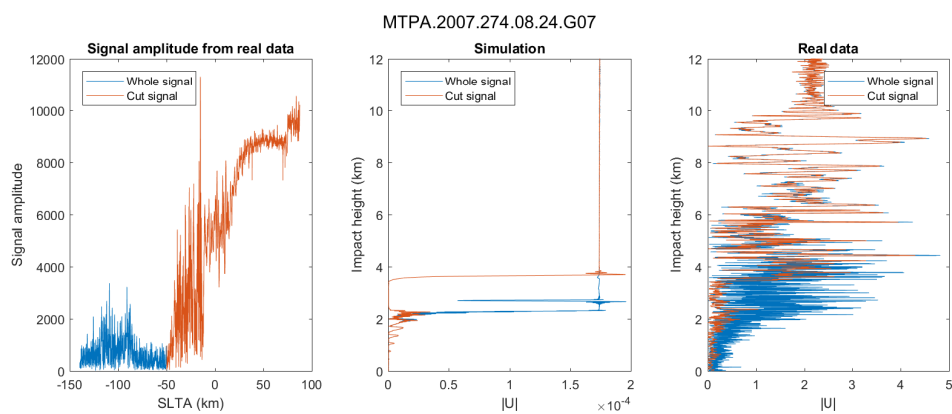
Figure 11. An event classified into category 3.
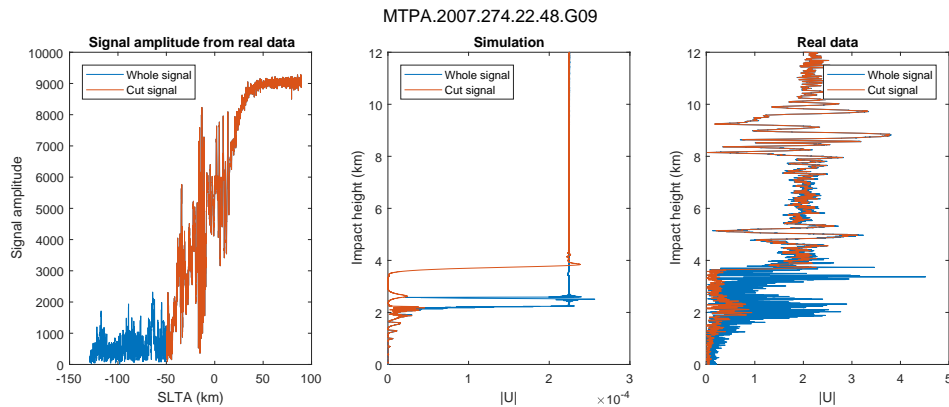
Figure 12. An event classified into category 4.

7 Conclusions

The results in this paper show that the signatures of surface reflections in GNSS RO measurements can be significantly enhanced when using the phase matching method by processing only an appropriately selected segment of the received signal. We can then identify reflection signatures even in cases where they are normally obscured by the direct signal's influence on
5 the phase matching amplitude. This signature enhancement is demonstrated by simulations and confirmed with real MetOp-A data.

The events containing reflected signals presented here are hand-picked to illustrate that the method works on real data. There are still questions that can only be answered by larger volumes of data, e.g. how this method compares with other methods used to identify reflections. Furthermore we observe that the reflection spikes vary greatly in shape. Additionally, simulated
10 reflection spikes always occur very close to the surface impact parameter, however in real measurements this is not always the case. The reason for these variabilities needs to be investigated. At this point we have only analyzed events over water, since we expect those reflections to be much clearer and numerous compared to over land.

When comparing the PM amplitudes of real and simulated signals, some interesting discrepancies were found. First, the characteristic dip in $|U|$ associated with a region of sharp gradient in the refractivity could not be identified in the real data,
15 being completely drowned in noise, or simply not present. Second, the levels of noise in the $|U|$ function tends to increase close to the Earth surface. As no noise was added to the simulations, it is not clear if this is due to instrument noise, or atmospheric disturbances. Third, peculiar oscillatory features at quite distinct heights were seen in the real data but not at all in the simulated. All these observations need further investigation before any conclusions can be drawn.

8   Data availability

The data from occultation events is collected from the COSMIC Data Analysis and Archive Center (CDAAC) web interface, found at the URL http://cdaac-www.cosmic.ucar.edu/cdaac/index.html.

Appendix A: Phase matching for reflected rays

5   It is not obvious that the phase matching method should work for reflected rays without modifications, but we will show that it does, under the assumption of reflections taking place on a perfectly smooth surface. First we will review the method used for phase matching of direct (non-reflected) rays, and then we will show that the result is the same for reflected rays. For the full details of the phase matching method the reader is referred to (Jensen et al., 2004).

A1   Direct rays

10   Under the assumption of spherically symmetric atmosphere we can use Bouger's rule

$$rn(r)\sin\phi = a \tag{A1}$$

where r is the distance from the Earth centre of curvature, n the refractive index, ϕ the angle the ray makes with the radial vector, and a the impact parameter. A ray is emitted from the GNSS satellite (at r_G) with angle ϕ_G, being smaller than π. The ray makes its closest approach to the Earth when $\phi = \pi/2$. The ray then exits the atmosphere and is received at the LEO

15   satellite (at r_L) with the angle ϕ_L. The total bending of the ray (measured positive towards the Earth) is given by the bending angle

$$\alpha(a) = -2a \int\limits_{a}^{\infty} \frac{1}{\sqrt{r^2 n(r)^2 - a^2}} \frac{d\ln n}{dr} dr \tag{A2}$$

The optical path length for the ray is given by the integral over the refractive index along the path of the ray

$$S = \int n(r) ds \tag{A3}$$

20   Where the term ds is an infinitesimal length along the ray. Under the spherical symmetry assumption the integral can be recast in a very attractive form, viz

$$S(t,a) = \sqrt{r_L(t)^2 - a^2} + \sqrt{r_G(t)^2 - a^2} - 2a^2 \int\limits_{a}^{\infty} \frac{1}{\sqrt{r^2 n(r)^2 - a^2}} \frac{d\ln n}{dr} dr - 2\int\limits_{a}^{\infty} \sqrt{r^2 n(r)^2 - a^2} \frac{d\ln n}{dr} dr \tag{A4}$$

The last term is connected to the bending angle in the following way

$$\int\limits_{a}^{\infty} \alpha(a')da' = -2\int\limits_{a}^{\infty} \sqrt{r^2 n(r)^2 - a^2}\frac{d\ln n}{dr}dr \tag{A5}$$

Using also the definition for the bending angle (eq. A2) we can write

$$S(t,a) = \sqrt{r_L(t)^2 - a^2} + \sqrt{r_G(t)^2 - a^2} + \alpha(a)a + \int\limits_{a}^{\infty} \alpha(a')da' \tag{A6}$$

5   The impact parameter is generally connected to a certain point in time, and certain values for r_L and r_G, in a complicated way. Whatever this connection may be the angles in the system must fulfill

$$\theta(t) + \phi_G + \phi_L - \pi = \alpha \tag{A7}$$

Where θ is the separation angle between the satellites. We can rewrite this using Bouger's rule

$$\theta(t) + \arcsin(a/r_L(t)) + \arcsin(a/r_G(t)) - \pi = \alpha \tag{A8}$$

10   For every value of a there will be a corresponding value for t. In that sense one could write the optical path length as a function of t only, viz

$$S(t) = \sqrt{r_L(t)^2 - a(t)^2} + \sqrt{r_G(t)^2 - a(t)^2} + \alpha(a(t))a(t) + \int\limits_{a(t)}^{\infty} \alpha(a')da' \tag{A9}$$

In the phase matching method we perform an integral for each value of a given impact parameter a_g where we wish to find the bending angle. The signal is given by

15   $$u(t) = |u(t)|\exp(ikS(t)) \tag{A10}$$

where k_0 is the wavenumber, and $i = \sqrt{-1}$. We subtract a geometrical model for the ray and form an integral as

$$U(a_g) = \int\limits_{t_0}^{t_E} |u(t)|\exp(ik(S(t) - S_g(t,a_g))) \tag{A11}$$

Where the geometrical ray is given by

$$S_g(t, a_g) = \sqrt{r_L(t)^2 - a_g^2} + \sqrt{r_G(t)^2 - a_g^2} + a_g \left(\theta(t) + \arcsin(a_g/r_L(t)) + \arcsin(a_g/r_G(t)) - \pi \right) \tag{A12}$$

The integral will get its main contribution from the point where there is a stationary phase point, characterized by

$$\frac{d}{dt}(S(t) - S_g(t, a_g)) = 0 \tag{A13}$$

5   The time derivative of S is given by

$$\frac{dS}{dt} = \frac{1}{r_L(t)} \frac{dr_L}{dt} \sqrt{r_L(t)^2 - a(t)^2} + \frac{1}{r_G(t)} \frac{dr_G}{dt} \sqrt{r_G(t)^2 - a(t)^2} + a(t) \frac{d\theta}{dt} \tag{A14}$$

Likewise, the time derivative of S_g is

$$\frac{dS_g}{dt} = \frac{1}{r_L(t)} \frac{dr_L}{dt} \sqrt{r_L(t)^2 - a_g^2} + \frac{1}{r_G(t)} \frac{dr_G}{dt} \sqrt{r_G(t)^2 - a_g^2} + a_g \frac{d\theta}{dt} \tag{A15}$$

Hence, the stationary phase point occurs where $a(t_g) = a_g$. At that point the difference in optical path length becomes

10   $$S(t_g) - S_g(t_g, a_g) = \int_{a_g}^{\infty} \alpha(a') da' \tag{A16}$$

And the integral is given by

$$U(a_g) = C(t_g) \exp\left(ik \int_{a_g}^{\infty} \alpha(a') da' \right) \tag{A17}$$

Where $C(t_g)$ is an amplitude factor depending on the signal amplitude and phase in the region around the stationary phase point. The bending angle as a function of impact parameter is thus found by taking the derivative of the phase of the function

15   U with respect to a_g, i.e.

$$\alpha(a_g) = -\frac{1}{k} \frac{d\angle U(a_g)}{da_g} \tag{A18}$$

A2 Reflected rays

For rays suffering reflection the Bouger's rule still applies, but the ray never reaches the point where $\phi = \pi/2$. Instead the ray is reflected at the point where $r = R_E$, where R_E is the Earth radius of curvature. Using the definition $R_E n(r_E) = a_E$ we find the angle the ray makes with the radial vector at reflection to be

$$\phi_E = \arcsin\left(\frac{a}{a_E}\right) \tag{A19}$$

Here we naturally assume that $a < a_E$, otherwise the ray would never reach the surface and be reflected. Since we assume the surface to be completely smooth, the radial vector is parallel to the surface normal, and since the incidence angle with respect to the surface normal is equal to the reflected ray angle with respect to the surface normal, we find that the ray angle after reflection is

$$\phi_E' = \pi - \phi_E \tag{A20}$$

We conclude that the ray suffers a negative bending of π radians due to the reflection. The total bending angle for a reflected ray is therefore given by

$$\alpha(a) = -2a \int\limits_{a_E}^{\infty} \frac{1}{\sqrt{r^2 n(r)^2 - a^2}} \frac{d\ln n}{dr} dr - \pi + 2\phi_E \tag{A21}$$

The integral for the optical path length becomes more complicated (although the derivation is straightforward)

$$S(t,a) = \sqrt{r_L(t)^2 - a^2} - \sqrt{a_E^2 - a^2} + \sqrt{r_G(t)^2 - a^2} - \sqrt{a_E^2 - a^2} - 2a^2 \int\limits_{a_E}^{\infty} \frac{1}{\sqrt{r^2 n(r)^2 - a^2}} \frac{d\ln n}{dr} dr - 2 \int\limits_{a_E}^{\infty} \sqrt{r^2 n(r)^2 - a^2} \frac{d\ln n}{dr} dr \tag{A22}$$

Taking the time derivative of this expression leads to the very same expression as Eq. A14. Hence, the stationary phase point again occurs where $a(t_g) = a_g$. At this point we have

$$S(t_g) - S_g(t_g, a_g) = -2\sqrt{a_E^2 - a_g^2} + a_g \pi - 2a_g \arcsin\left(\frac{a_g}{a_E}\right) - 2 \int\limits_{a_E}^{\infty} \sqrt{r^2 n(r)^2 - a_g^2} \frac{d\ln n}{dr} dr \tag{A23}$$

This is the term that appears in the phase of the phase matching function $U(a_g)$. Taking the derivative with respect to a_g leads to

$$\frac{d}{da_g}\left(S(t_g) - S_g(t_g, a_g)\right) = -2a_g \int\limits_{a_E}^{\infty} \frac{1}{\sqrt{r^2(r)n^2 - a_g^2}} \frac{d\ln n}{dr} dr + \pi - 2\arcsin\left(\frac{a_g}{a_E}\right) \tag{A24}$$

Which is the bending angle for a reflected ray as given in Eq. (A21) Consequently the phase matching method works in the exact same way for direct and reflected rays. It should be stressed that these derivations are only valid when the Earth surface can be considered smooth. When the surface is not smooth the incoming ray will change impact parameter upon reflection. Due to this the expression for the optical path length becomes a function of the old and new impact parameter, and the simple

5   geometrical ray model used in the phase matching method cannot lead to a stationary phase point. This is basically a case of multipath in the impact parameter domain. It may be argued though that this is of little consequence for real measurements since the occultation measuring instrument will not record signals that deviate too strongly from direct rays, as they quite rapidly become heavily Doppler shifted with increasing reflection angle. For this reason reflected signals will only be seen at impact parameters that are very close to the value at the Earth surface. These rays are of grazing incidence, and under such

10   circumstances the surface may always be considered as flat (Beekmann and A, 1963).

Author contributions. J. Rasch, T. Sievert, A. Carlström and M. I. Pettersson designed the study and T. Sievert performed the simulations and processing. T. Sievert prepared the manuscript with contributions from all co-authors. J. Rasch performed the calculations for the reflection model and wrote the appendix.

Acknowledgements. This research was supported by The Swedish National Space Board and The Knowledge Foundation (KKS).

References

Beekmann, P. and A, S.: The Scattering of Electromagnetic Waves from Rough Surfaces, International Series of Monographs on Electromagnetic Waves, Pergamon Press, 1963.

Benzon, H. H. and Gorbunov, M. E.: Description of a wave propagator and radio occultation simulations, EUMETSAT study: Optimisation of tracking strategies for radio occultations, version 2.2.4, 2012.

Benzon, H. H., Nielsen, A. S., and Olsen, L.: An atmospheric wave optics propagator - theory and application, Scientific report 03-01, Danish Meteorological Institute, 2003.

Beyerle, G., Hocke, K., Wickert, J., Schmidt, T., Marquardt, C., and Reigber, C.: {GPS} radio occultations with {CHAMP}: {A} radio holographic analysis of {GPS} signal propagation in the troposphere and surface reflections, Journal of Geophysical Research-Atmospheres, 107, 4802, doi:10.1029/2001JD001402, 2002.

Boniface, K., Aparicio, J. M., and Cardellach, E.: Meteorological information in GPS-RO reflected signals, Atmos. Meas. Tech, 4, 1397–1407, doi:10.5194/amt-4-1397-2011, www.atmos-meas-tech.net/4/1397/2011/, 2011.

Cardellach, E. and Oliveras, S.: Assessment of a potential reflection flag product, ROM SAF Report 23, Radio Occultation Meteorology Satellite Application Facility, www.romsaf.org, 2016.

Gorbunov, M.: Development of wave optics code for the retrieval of bending angle profiles for reflected rays, ROM SAF Visiting Scientist Report 27, Radio Occultation Meteorology Satellite Application Facility, www.romsaf.org, 2016.

Healy, S.: The use of the GPS radio occultation reflection flag for NWP applications, ROM SAF Visiting Scientist Report 22, Radio Occultation Meteorology Satellite Application Facility, www.romsaf.org, 2015.

Healy, S. B.: Optimizing Tracking Strategies for Radio Occultation. Task 1 - the Profile Dataset, Tech. rep., ECMWF/EUMETSAT, 2012.

Hocke, K., Pavelyev, A. G., Yakovlev, O. I., Barthes, L., and Jakowski, N.: Radio occultation data analysis by the radioholographic method, Journal of Atmospheric and Solar-Terrestrial Physics, 61, 1169–1177, doi:10.1016/S1364-6826(99)00080-2, 1999.

Jensen, A. S., Lohmann, M. S., Nielsen, A. S., and Benzon, H.-H.: Geometrical optics phase matching of radio occultation signals, Radio Science, 39, RS3009–RS3009, doi:10.1029/2003RS002899, 2004.

Kursinski, E. R., Hajj, G. A., Leroy, S. S., and Herman, B.: The GPS radio occultation technique, Terrestrial, Atmospheric and Oceanic Sciences, 11, 53–114, 2000.

Levy, M.: Parabolic Equation Methods for Electromagnetic Wave Propagation, Electromagnetics and Radar Series, Institution of Electrical Engineers, 2000.

Pavelyev, A. G., Igarashi, K., Pavelyev, D. A., and Hocke, K.: Radioholographic method for observation of reflections from the {Earth}'s surface and of wave structures based on occultations, Journal of Communications Technology and Electronics, 47, 609–614, 2002.

Rasch, J.: Theory and Implementation of an End-to-End Radio Occultation Simulator, Technical Report, Earth and Space Sciences, no 10, Chalmers University of Technology, 2014.

Tukey, J. W.: An introduction to the calculations of numerical spectrum analysis, Spectral analysis of time series, 25, 1967.

Yunck, T. P., Liu, C.-H., and Ware, R.: A history of GPS sounding, Terrestrial, Atmospheric and Oceanic Sciences, 11, 1–20, 2000.